Journal Pre-proof

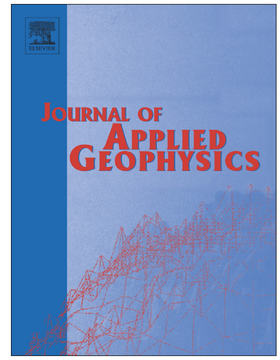

Laterally constrained inversion (LCI) of multi-configuration EMI data with tunable sharpness

Tim Klose, Julien Guillemoteau, Giulio Vignoli, Jens Tronicke

PII: S0926-9851(21)00267-6

DOI: https://doi.org/10.1016/j.jappgeo.2021.104519

Reference: APPGEO 104519

To appear in: *Journal of Applied Geophysics*

Please cite this article as: T. Klose, J. Guillemoteau, G. Vignoli, et al., Laterally constrained inversion (LCI) of multi-configuration EMI data with tunable sharpness, *Journal of Applied Geophysics* (2021), https://doi.org/10.1016/j.jappgeo.2021.104519

Laterally Constrained Inversion (LCI) of multi-configuration EMI data with tunable sharpness

Tim Klose[a,*], Julien Guillemoteau[a], Giulio Vignoli[b], Jens Tronicke[a]

[a] University of Potsdam, Institute of Geosciences, Karl-Liebknecht-Str. 24-25, 14476 Potsdam-Golm, Germany

[b] University of Cagliari, Department of Civil, Environmental Engineering and Architecture, 09123 Cagliari, Italy & Geological Survey of Denmark and Greenland (GEUS), Department of Groundwater and Quaternary Geology Mapping, 8000 Aarhus, Denmark

Abstract

Frequency-domain electromagnetic (FDEM) data are commonly inverted to characterize subsurface geoelectrical properties using smoothness constraints in 1D inversion schemes assuming a layered medium. Smoothness constraints are suitable for imaging gradual transitions of subsurface geoelectrical properties caused, for example, by varying sand, clay, or fluid content. However, such inversion approaches are limited in characterizing sharp interfaces. Alternative regularizations based on the minimum gradient support (MGS) stabilizers can, instead, be used to promote results with different levels of smoothness/sharpness selected by simply acting on the so-called focusing parameter. The MGS regularization has been implemented for different kinds of geophysical data inversion strategies. However, concerning FDEM data, the MGS regularization has only been implemented for vertically constrained inversion (VCI) approaches but not for laterally constrained inversion (LCI) approaches.

We present a novel LCI approach for FDEM data using the MGS regularization for the vertical and lateral direction. Using synthetic and field data examples, we demonstrate that our approach can efficiently and automatically provide a set of model solutions characterized by different levels of sharpness and variable lateral consistencies. In terms of data misfit, the obtained set of

*Corresponding author

Email address: `tim.klose@uni-potsdam.de` (Tim Klose)

solutions contains equivalent models allowing us also to investigate the non-uniqueness of FDEM data inversion.

Keywords: Frequency-domain electromagnetics, Laterally constrained inversion, Minimum gradient support regularization, Peat characterization

1. Introduction

Portable electromagnetic induction (EMI) sensors using harmonic source waveforms (also known as frequency-domain electromagnetics - FDEM) are commonly used to characterize near-surface geoelectrical properties. Such methods are used in various applications including archaeological prospection (De Smedt et al., 2014; Dabas et al., 2016; von Hebel et al., 2021), precision agriculture (Jadoon et al., 2015; Rudolph et al., 2016; Brogi et al., 2019), hydrological studies (Vereecken et al., 2015; von Hebel et al., 2014; Rezaei et al., 2016; Robinet et al., 2018), and environmental studies including the exploration of peat deposits (Altdorff et al., 2016; Beucher et al., 2020; Clément et al., 2020; McLachlan et al., 2020). Modern single-frequency, multi-configuration sensors can simultaneously sense the subsurface electrical conductivity for different volumes of investigation. Thus, the resulting data sets allow the reconstruction of heterogeneous models through data inversion.

For their computational costs, 2D/3D inversion of EMI data have been used for the reconstruction of relatively small problems (Sasaki et al., 2010; Pérez-Flores et al., 2012; Yi & Sasaki, 2015; Benech et al., 2016). However, recently, new Fourier-based approaches (Guillemoteau & Tronicke, 2016; Guillemoteau et al., 2017a) made them practical for large data sets. For characterizing subsurface formations of relatively large lateral extent, EMI data are commonly interpreted using 1D layered medium inversion approaches as they offer a good balance between robustness and computational expense for this kind of target (Saey et al., 2012; Grellier et al., 2013; von Hebel et al., 2014; Davies et al., 2015; Guillemoteau et al., 2016; McLachlan et al., 2021). Like many other geophysical inverse problems, EMI data inversion is typically ill-posed (Tikhonov & Arsenin, 1977). To cope with this, a stabilizing term formalizing the available prior information is introduced in the objective functional to be minimized. One popular stabilizer consists of a smoothness constraint term (Constable et al., 1987). As commonly used in vertically constrained inversion (VCI) approaches, the smooth constraints limit the variability between the parameter values characterizing the adjacent layers within the 1D model. To enforce lateral consistency of the inversion result (i.e., in the neighborhood of 1D models), laterally constrained inversion (LCI) approaches are used (Auken & Christiansen, 2004). Here, the neighboring 1D models are linked by lateral (smoothness) constraints (Auken et al., 2008; Viezzoli et al., 2010). Such LCI approaches have also been successfully applied to FDEM data (Christiansen et al., 2016; Frederiksen et al., 2017). Nevertheless, such approaches are limited if sharp interfaces (e.g., geological boundaries between two distinct formations) are present in the subsurface (Linde et al., 2015; Zhdanov & Tolstaya, 2004). One regularization strategy to enforce a sharp or blocky solution is based on the minimum gradient support (MGS) method (Portniaguine & Zhdanov, 1999; Zhdanov, 2002). Within the MGS regularization, a focusing parameter controls the characteristics of the used stabilizer; i.e., a small parameter value promotes sharp solutions while a large value promotes smoother models (Vignoli et al., 2015; Deidda et al., 2020; Vignoli et al., 2021). The MGS regularization has been implemented in several inversion approaches for other geophysical methods. For example, it has been successfully used for the inversion of gravity data (Last & Kubik, 1983), electrical resistivity data (Blaschek et al., 2008; Fiandaca et al., 2015; Thibaut et al., 2021), seismic dispersion curves (Vignoli et al., 2021), traveltime data sets (Zhdanov et al., 2006; Vignoli et al., 2012), and time-domain electromagnetic data (Ley-Cooper et al., 2015; Vignoli et al., 2015, 2017). For FDEM data, VCI strategies using the MGS regularization have been presented by Deidda et al. (2020). In contrast, to our knowledge, this is the first implementation of MGS-LCI for FDEM data.

Depending on the application, targeted structures may show different lateral consistency (e.g., tens to hundreds of meters of soil layers versus meter-sized archaeological artifacts) and variable interface sharpness (e.g., gradual variations in fluid or sand content within a single geological unit versus a sharp, distinct interface between two geological units). The inverse problem is often non-unique regarding these characteristics. It is therefore necessary to develop rapid and rather exhaustive data inversion procedures, which automatically provide a solution for different geological settings.

In this study, we present a novel LCI approach for FDEM data based on the MGS regularization in both the vertical and the lateral direction. Our inversion strategy relies on a gradient-based inversion procedure which converges for arbitrary model sharpness and lateral consistency and, thus, efficiently and automatically provides a set of equivalent solutions (in terms of data misfit). In the following, we provide the details of this inversion strategy. Then we evaluate our proposed method using 1D and 2D synthetic data sets computed with full non-linear forward modeling approaches. Finally, we apply such a multi-solution strategy to a field data set acquired in Paulinenaue, Germany, to explore and characterize peat deposits.

2. Theory

EMI multi-configuration sensors typically provide LIN (low induction number) apparent conductivity σ_a data calculated after McNeill (1980). In the presented inversion procedure, we convert the given LIN conductivities back to out of phase (OP) data and to robust σ_a values using the full homogeneous half-space theory (Wait, 1962) as described in Guillemoteau et al. (2016). Similar transformations are commonly used in electrical resistivity tomography and have also been used for time-domain electromagnetic approaches (Christensen, 1995; Guillemoteau et al., 2011, 2012). They allow to remove the effect of the acquisition parameters (e.g., frequency, configuration or sensor clearance) from the data. The resulting modified data space used for the inversion thereby only contains information related to the subsurface properties. Following Johansen (1977), we invert the logarithm of σ_a. The vector of the observed data $\boldsymbol{d^{obs}}$ is given by

$$\boldsymbol{d^{obs}} = [log\sigma_{a,1}, log\sigma_{a,2}, \ldots, log\sigma_{a,N_d}]^T, \tag{1}$$

where N_d is the number of data points. When performing a 1D inversion for one sounding, N_d is equal to the number of configurations N_c. When simultaneously inverting several soundings, N_d is equal to the number of configurations N_c times the number of soundings N_s. Similarly, we define the model parameter vector $\boldsymbol{m}$ using the logarithmic conductivities of the individual layers by

$$\boldsymbol{m} = [log\sigma_1, log\sigma_2, \ldots, log\sigma_{N_m}]^T \tag{2}$$

where N_m is the number of model parameters. If the inversion is performed for one sounding, N_m is equal to the number of layers N_l. If the inversion is performed for N_s soundings, $\boldsymbol{m}$ is a vector containing the N_s times N_l elements.

In our inversion approach, to obtain an estimated solution of the model parameters explaining the observed data, we minimize the following objective function ϕ:

$$\phi = \sum_{i=1}^{N_d} [(\boldsymbol{W d^{obs}})_i - (\boldsymbol{W d^{mod}})_i]^2 + \alpha \sum_{j=1}^{N_m} \left[\frac{(\boldsymbol{D_z m})_j^2}{(\boldsymbol{D_z m})_j^2 + \epsilon^2} + w \frac{(\boldsymbol{D_x m})_j^2}{(\boldsymbol{D_x m})_j^2 + \epsilon^2} \right]. \tag{3}$$

The first sum describes the data misfit; i.e., it characterizes the difference between the observed data $\boldsymbol{d^{obs}}$ and the modeled data $\boldsymbol{d^{mod}}$. $\boldsymbol{W}$ is a diagonal matrix containing data weights, which are set depending on the characteristics of the assumed data uncertainties. The second sum of equation 3 is the regularization term. The importance of this sum with respect to the data misfit sum is controlled by the scalar value α. Within this second sum, the two terms describe the model constraints in the vertical (z) and lateral (x) direction, respectively. The relative level of the lateral constraints is controlled by the scalar value w. Having a different weight between the spatial components is not unusual (in this respect, for example, Auken et al., 2015) as the correlation lengths are generally different. The matrices $\boldsymbol{D_z}$ and $\boldsymbol{D_x}$ are first-order spatial differential operators for corresponding neighboring model elements of $\boldsymbol{m}$ in the vertical and lateral direction, respectively. The scalar value ϵ avoids singularity occurrences when

$(\boldsymbol{D_z m})_j^2 = 0$ or $(\boldsymbol{D_x m})_j^2 = 0$, and defines the threshold to consider the variation of the model parameters significant (e.g., Vignoli et al., 2021). Due to the latter fact, ϵ is commonly referred as the focusing parameter.

We minimize equation 3 using the following iterative formula (Constable et al., 1987):

$$\boldsymbol{m}_{s+1} = [\boldsymbol{J}^T(\boldsymbol{m}_s)\boldsymbol{C_d}\boldsymbol{J}(\boldsymbol{m}_s)+\alpha_s\boldsymbol{S}(\boldsymbol{m}_s)]^{-1}\boldsymbol{J}^T(\boldsymbol{m}_s)\boldsymbol{C_d}[\boldsymbol{d^{obs}}-\boldsymbol{f}(\boldsymbol{m}_s)+\boldsymbol{J}(\boldsymbol{m}_s)\boldsymbol{m}_s], \tag{4}$$

where s denotes the iteration number, $\boldsymbol{J}$ is the Jacobian of the problem, $\boldsymbol{C_d} = \boldsymbol{W}^T\boldsymbol{W}$ is the data weighting matrix, $\boldsymbol{S}$ the regularization matrix described below, and $\boldsymbol{f}$ represents the 1D forward modeling of the data. Here, $\boldsymbol{f}$ is the logarithm of the full 1D non-linear forward modeling of σ_a, which consists of two steps:

$$\boldsymbol{m}_s \xrightarrow{\ 1\ } \boldsymbol{OP}(\boldsymbol{m}_s) \xrightarrow{\ 2\ } log(\boldsymbol{\sigma_a}(\boldsymbol{OP})).$$

Transformation 1 corresponds to the full 1D forward modeling of the OP data, and transformation 2 is the conversion of the OP data into σ_a data using the full homogeneous half-space theory. The latter transformation is univocal and reversible in the low to moderate induction number range, which is the operating domain for portable rigid-boom mono-frequency sensors as considered in this study. The Jacobian $\boldsymbol{J}$ of the logarithm of $\sigma_{a,i}$ with respect to the conductivity of the layer j can be calculated, by simply applying the differentiation chain rule, as (Guillemoteau et al., 2016)

$$\boldsymbol{J}_{ij}\big|_\sigma = \frac{\sigma_j}{\sigma_{a,i}}\ \frac{\partial\sigma_{a,i}}{\partial OP_i}\ \frac{OP_i(\sigma+\Delta\sigma_j)-OP_i(\sigma)}{\Delta\sigma_j}, \tag{5}$$

where the derivative $\frac{\partial\sigma_{a,i}}{\partial OP_i}$ is numerically evaluated when converting OP data into robust σ_a data. The diagonal entries of the $N_d \times N_d$ data weighting matrix $\boldsymbol{C_d}$ are set depending on the data uncertainties after Tarantola (2005) which, for the logarithmic space, is calculated by (Guillemoteau et al., 2017b)

$$(\boldsymbol{C_d})_{ii} = log(1+\boldsymbol{\delta}_i)^{-2}, \tag{6}$$

where $\boldsymbol{\delta}_i$ is the relative uncertainty of the σ_a data. In practice, when assuming relative uncertainties, we directly set $\boldsymbol{\delta}_i$ to the required value. On the other hand, to model absolute uncertainties $\boldsymbol{\Delta\sigma_{a,i}}$ in S/m, we set $\boldsymbol{\delta}_i$ to

$$\boldsymbol{\delta}_i = \frac{\boldsymbol{\Delta\sigma_{a,i}}}{\boldsymbol{\sigma_{a,i}}}. \tag{7}$$

In equation 4, the regularization matrix $\boldsymbol{S}$ is defined as:

$$\boldsymbol{S} = \frac{1}{\sum diag(\boldsymbol{L_z^T L_z})} \cdot [\boldsymbol{L_z^T L_z} + w\boldsymbol{L_x^T L_x}], \tag{8}$$

where the matrices $\boldsymbol{L_z}$ and $\boldsymbol{L_x}$ are the MGS operators for the vertical and lateral direction:

$$\boldsymbol{L}_z = \frac{\boldsymbol{D_z}}{\sqrt{[\boldsymbol{D_z m}_s]^2 + \epsilon^2}} \quad and \quad \boldsymbol{L_x} = \frac{\boldsymbol{D_x}}{\sqrt{[\boldsymbol{D_x m}_s]^2 + \epsilon^2}}. \tag{9}$$

The MGS operator is model-dependent. As a consequence, the optimal regularization weight α might vary during the iterations primarily depending on $\boldsymbol{m}_s$. In equation 8, the scaling by the trace of $\boldsymbol{L_z^T L_z}$ is applied to make the α-search general and avoid the need for adjustments every time the range of the conductivity and/or its spatial derivatives change. The optimal α value is automatically found at each iteration by computing the root mean square relative error (RMSRE) between the observed and modeled σ_a as a function of α (the α-search is performed over several orders in a logarithm scale beginning with a large value and decreasing it until the RMSRE value is increasing). In our inversion strategy, the starting model $\boldsymbol{m_0}$ contains N_s homogeneous media $\boldsymbol{M_k}$ defined as the mean of the observed robust σ_a data for each sounding k:

$$\boldsymbol{m_0} = [\boldsymbol{M_1}, \ldots, \boldsymbol{M_k}, \ldots, \boldsymbol{M_{N_s}}]^T, \tag{10}$$

where, for all components of the k-th 1D conductivity model, each layer has a conductivity equal to

$$\boldsymbol{M_{k,l}} = log(\boldsymbol{\bar{\sigma}^{obs}_{a,k}}) \quad for\ l = 1, \ldots, N_l. \tag{11}$$

It is important to highlight here that for the case of portable single-frequency instruments, which operate at low to moderate induction numbers, the starting model is by definition not a critical choice, and thereby nor a relevant parameter to be explored as the vertical sensitivities are very poorly dependent on the model of conductivity (Guillemoteau & Tronicke, 2016). The estimated solution $\boldsymbol{m}$ of the inverse problem is found, when 1) the RMSRE is below a threshold, which is set according to the assumed noise/uncertainties, or 2) the relative change in RMSRE is below a certain threshold, which we set to 25 % of the RMSRE.

3. 1D synthetic data example

With this first example, we want to demonstrate the basic principles of the presented inversion procedure using a 1D synthetic data set consisting of a single sounding ($N_s = 1$). We consider the case of a four-configuration instrument operating at a single frequency of 9 kHz placed at 0.25 m above ground. The four configurations consist of two horizontal coplanar (HCP) and two perpendicular (PERPx) configurations with coil spacings of 1 m, 2 m, 1.1 m, and 2.1 m, respectively. Here, we perform a noise-free synthetic test to focus on the characteristics of the implemented model constraints. The used subsurface model consists of two layers (Figure 1): A conductive layer at the top with $\sigma_1 = 0.1$ S/m, and a more resistive layer below with $\sigma_2 = 0.01$ S/m. The interface between these two layers is located at a depth of 0.5 m.

For the inversion of this synthetic sounding, we set the number of layers N_l in the model space to 50 with increasing thickness towards deeper layers up to a depth of 4 m. Because we analyze a single sounding, we consider vertical constraints only in equation 3 and, thus, we follow a VCI strategy. Because all other parameters are fixed or automatically found within the inversion procedure, only two user-specified parameters control the inversion result. These are the scalar value ϵ and the assumed data uncertainty $\boldsymbol{\delta}_i$ (see also equations 6, 7 and 9).

3.1. *Influence of ϵ on the inversion result*

To show the influence of ϵ on the inversion result, we set the assumed noise $\boldsymbol{\Delta\sigma_{a,i}}$ to a constant absolute value of 0.1 mS/m. This value is indeed quite small and definitely far from being realistic, but, here, the point of this exercise is to verify the impact of the focusing parameter values on the inversion. The inversion results for different ϵ values are shown in Figure 1. The RMSRE of all results are in the same range (between 0.22% and 0.36%); i.e., all of the shown results can be considered as equivalent models. In general, a small value of ϵ, for this example 0.01, produces a sharp/blocky inversion result. In fact, the name minimum gradient support indicates that the chosen stabilizer tends to minimize the support of the spatial model gradient (i.e. the area in which the gradient is not vanishing). The focusing parameter defines, in a broad sense, when a conductivity variation is small enough to be neglected (so it defines the support). On the other hand, large values of the spatial variation of the model are not particularly penalized (as, on the contrary, it happens in the standard Occam's inversion). Using a high ϵ value, the regularization term aims at minimizing the gradient of the model parameter vector equally over the whole model space. Thus, in this first synthetic example, high ϵ values favor a smooth inversion result.

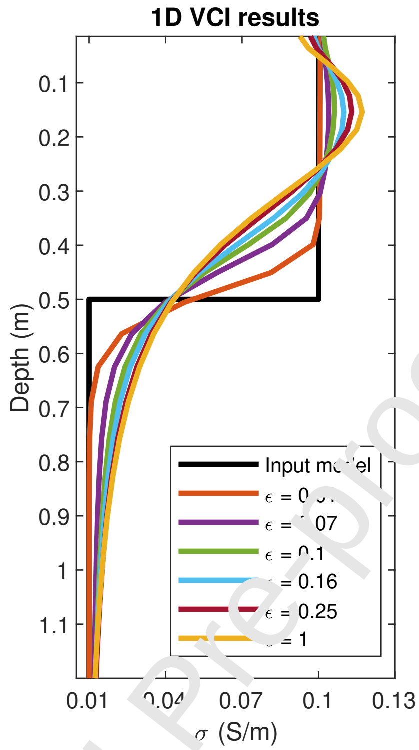

Figure 1: 1D VCI results for several values of ϵ. The input model (black line) used for forward modeling the synthetic data consists of a conductive top layer with $\sigma_1 = 0.1$ S/m and a second, more resistive layer with $\sigma_2 = 0.01$ S/m. The interface is located at a depth of 0.5 m.

3.2. Influence of the assumed noise level on the inversion result

The MGS operator describes an iterative sharpening procedure which is related to the number of iterations. Therefore, a change in the assumed noise level, which influences the number of iterations needed to solve a specific inversion problem, results in different levels of model sharpness. To illustrate this link, the inversion results for each iteration using $\epsilon = 0.01$ are shown in Figure 2a (see also orange line in Figure 1). In Figure 2b, we show the corresponding RMSRE values for each iteration. In this example, the assumed absolute noise $\boldsymbol{\Delta\sigma_{a}}_{,i}$ is set to 0.1 mS/m. We obtain the logical final inversion result after six iterations. Starting with a homogeneous initial model, the level of sharpness increases at each iteration; i.e., the size of the gradient variations along the model parameter vector is increasing. The RMSRE value decreases with each iteration and, using a noise level of 0.1 mS/m, the corresponding RMSRE threshold of 0.25% (red dotted line in Figure 2b) is reached after six iterations. If we assume a noise level of 1 mS/m, we reach the corresponding RMSRE threshold of 2.5% (blue dotted line in Figure 2b) after four iterations. Comparing the models obtained after four and six iterations (blue and red line in Figure 2a) illustrates that a higher value of the assumed noise level decreases the number of iterations needed to obtain a final inversion result but, decreases the level of sharpness in the result.

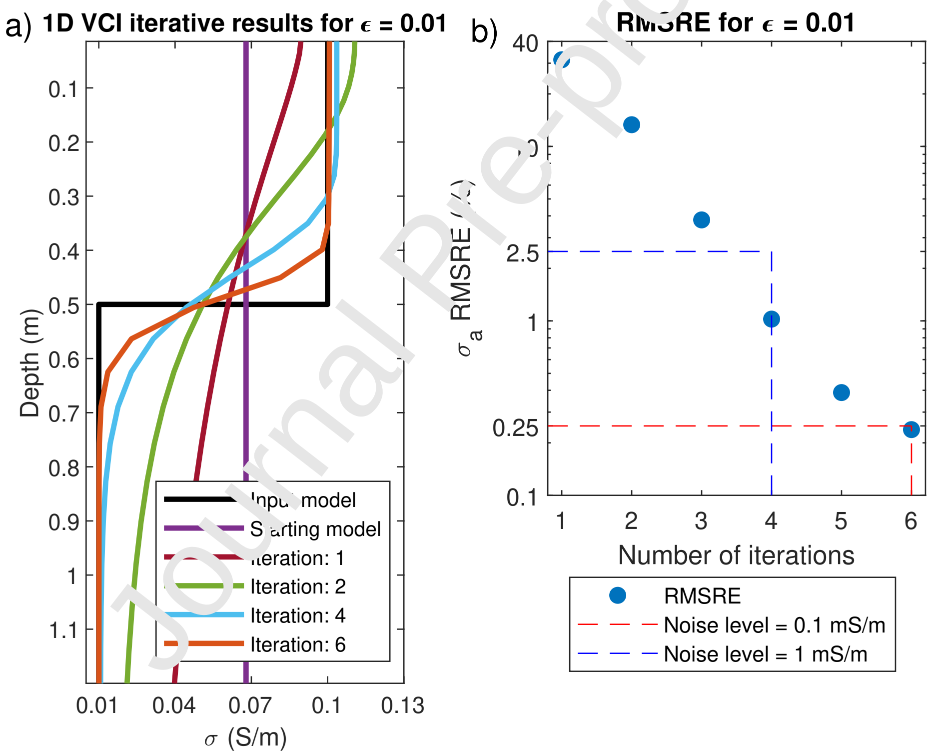

Figure 2: a) 1D VCI results for several iterations using $\epsilon = 0.01$. The input model (black line) used for forward modeling the synthetic data consists of a conductive top layer with $\sigma_1 = 0.1$ S/m and a second, more resistive layer with $\sigma_2 = 0.01$ S/m. The interface is located at a depth of 0.5 m. b) The RMSRE evolution with each iteration corresponding to the results shown in a. The dotted lines indicate two different RMSRE thresholds, using different absolute values of noise.

4. 2D synthetic data example

Typical field data sets consist of thousands of soundings across large areas (e.g., several hectars) along numerous profile lines. In this second synthetic example, we use the same four-configuration instrument as used in the first example and compute a 2D synthetic data set across a subsurface model showing lateral variations in electrical conductivity. For simulating this data set, we use a 3D non-linear forward modeling method based on the finite volume approach (Haber, 2014). The synthetic data set consists of 215 four-configuration soundings with a in-line spacing of 0.6 m, resulting in $N_d = 860$. The input subsurface model consists of two layers separated by an oscillating interface. Comparable to the fist synthetic example, the electrical conductivity of the upper layer is 0.1 S/m and 0.01 S/m for the lower layer. The interface depth starts with a constant value of 0.3 m and varies between 0.3 m and 1.5 m with increasing wavelengths towards the end of the profile (see Figure 3a). This input model can be separated into two parts. The first part, up to approximately X = 70 m, can be regarded as a 2D context, because the wavelength of the interface undulations is below or equal to the lateral footprint of the used coil configurations, which can be approximated by 1.5 times the maximum coil spacing as learned for example by studying the 3D sensitivity patterns of the configurations (e.g., Guillemoteau & Tronicke, 2015). The second part of the profile (at around X = 70 m and more) can be regarded as a quasi-1D context. We add uncorrelated noise of ±1 mS/m to the synthetic LIN σ_a data, and define the value of the assumed noise $\boldsymbol{\Delta\sigma_{a,i}}$ for the inversion at the same level. In accordance to the first synthetic example, we set the number of layers N_l to 50 with increasing thickness towards deeper layers up to a depth of 4 m.

First, we perform a VCI of the synthetic data set for two different ϵ values, where the individual soundings are inverted independently and, thus, the resulting solutions are stitched together for generating a pseudo-2D model. In Figure 3, we show the inversion results of a VCI for $\epsilon = 0.01$ (Figure 3b) representing a sharp result, and for $\epsilon = 1$ (Figure 3c) representing a smooth result.

The OP data and the corresponding robust σ_a data misfits are shown in Figure 3d-e. Both results provide a good image of the input model (see Figure 3a) as also indicated by the black lines in Figure 3b-c representing the location of the true interface. Major discrepancies are found in the first part of the profile, which corresponds to the 2D context. These results are expected and are used here to illustrate the limitations of the 1D assumption regarding the lateral resolution capabilities. The major difference between the inversion results obtained using different ϵ values can be seen in the transition zone between the two layers. A lower value of ϵ shows a higher gradient in this zone. The two solutions are indeed comparable as they are characterized by a similar level of data fitting (Figure 3f). In the VCI results, the lateral variations in the electrical conductivity values, especially visible within the bottom layer, show a lack of lateral consistency, which can be tackled when including lateral constraints in the inversion procedure.

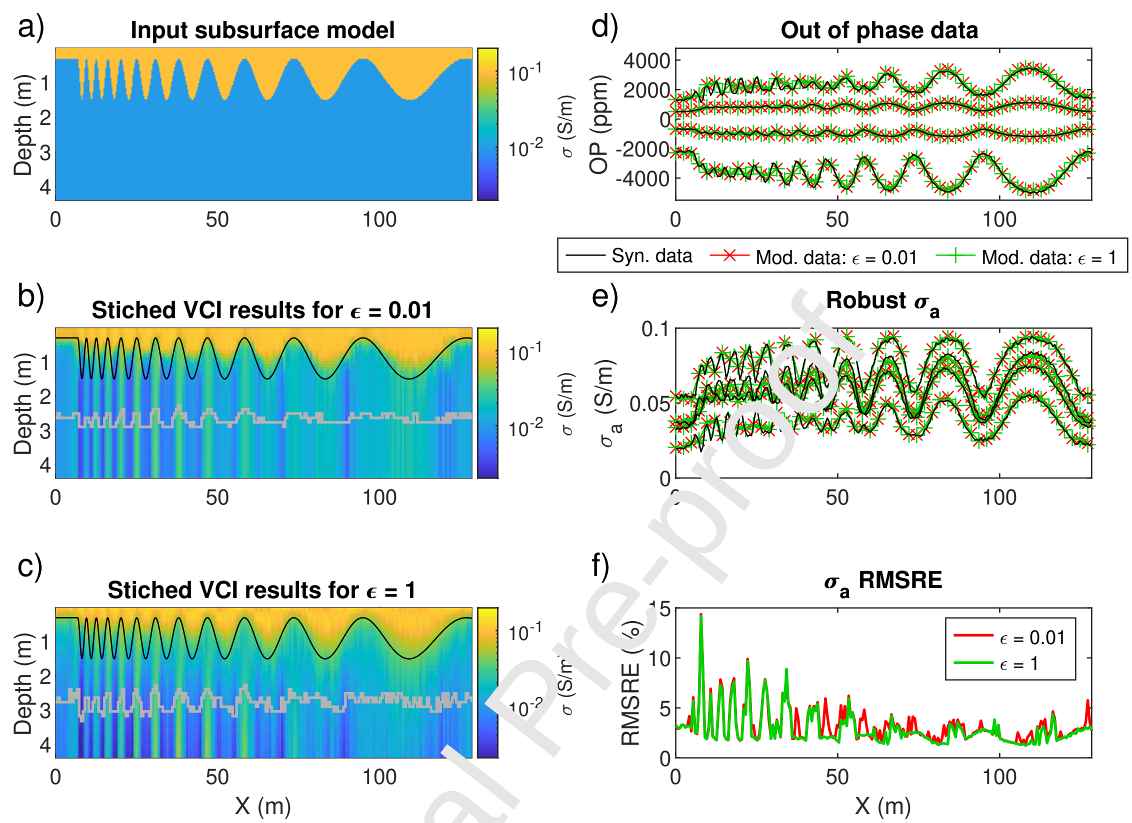

Figure 3: a) Input subsurface model used to compute the synthetic data. b) Stitched VCI result using $\epsilon = 0.01$. c) Stitched VCI result using $\epsilon = 1$. In b) - c), the black line indicates the true interface depth and the gray line indicates an estimated maximum depth of investigation for this scenario. d) OP data of the second synthetic example (black line) compared to the data from two VCI results. e) Converted robust σ_a of the second synthetic example (black line) compared to the data from two VCI results. f) RMSRE misfit for the two VCI results.

When using our LCI approach, all soundings are inverted together and we have to consider two regularization parameters (ϵ and w, see also equation 3). The value for w defines the weight of the lateral constraints; i.e., a higher value enforces a larger lateral coherence. Similar to Figure 3, we show in Figure 4 the LCI results for two selected ϵ values. We tested different w values between 0 and 1. In practice, an acceptable value can be easily and rapidly found with few tests by checking if the model of the first iteration shows lateral variations which are consistent with the lateral distribution of the data. For this example, such strategy yielded a value of $w = 0.3$. Compared to the VCI case (Figure 3), the lateral consistency in the LCI results increases (Figure 4) and the difference between the sharp (Figure 4b) and the smooth (Figure 4c) inversion result is more obvious. The data misfit for both LCI results are similar. Compared to the misfit curves shown in Figure 3, the misfits for the LCI results are higher for the first part of the profile and lower for the second part of the profile. Thus, in the 2D context part of the profile (where lateral variations are more pronounced), enforcing lateral coherence increases the mismatch between calculated and observed data. On the other hand, in the 1D context part of the profile (where the lateral variations have characteristic lengths larger than the instrument footprint), imposing lateral constraints improves the performance in terms of local data fitting. In this part of the profile, the LCI models also show a better reconstruction of the input subsurface model compared to the VCI results. To demonstrate this in more detail, we show zoom-ins of the inversion results for all four cases (two VCI and two LCI results) in Figure 5. We notice here that the lateral consistency increases when adding lateral constraints (from left to right column of Figure 5) and the level of sharpness increases when decreasing the value of w (from bottom to top line of Figure 5).

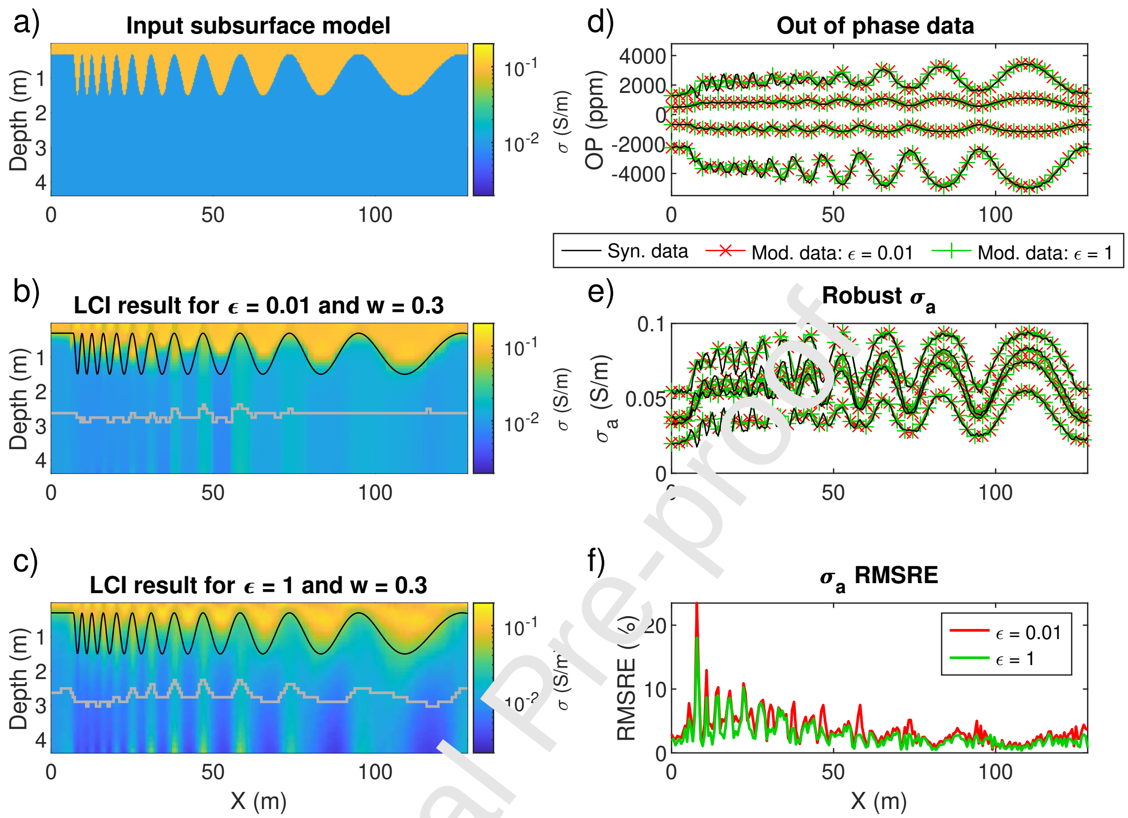

Figure 4: a) Input subsurface model used to compute the synthetic data. b) LCI result using $\epsilon = 0.01$ and $w = 0.3$. c) LCI result using $\epsilon = 1$ and $w = 0.3$. In b) - c), the black line indicates the true interface depth and the gray line indicates an estimated maximum depth of investigation for this scenario. d) OP data of the second synthetic example (black line) compared to the data from two LCI results. e) Converted robust σ_a of the second synthetic example (black line) compared to the data from two LCI results. f) RMSRE misfit for the two LCI results.

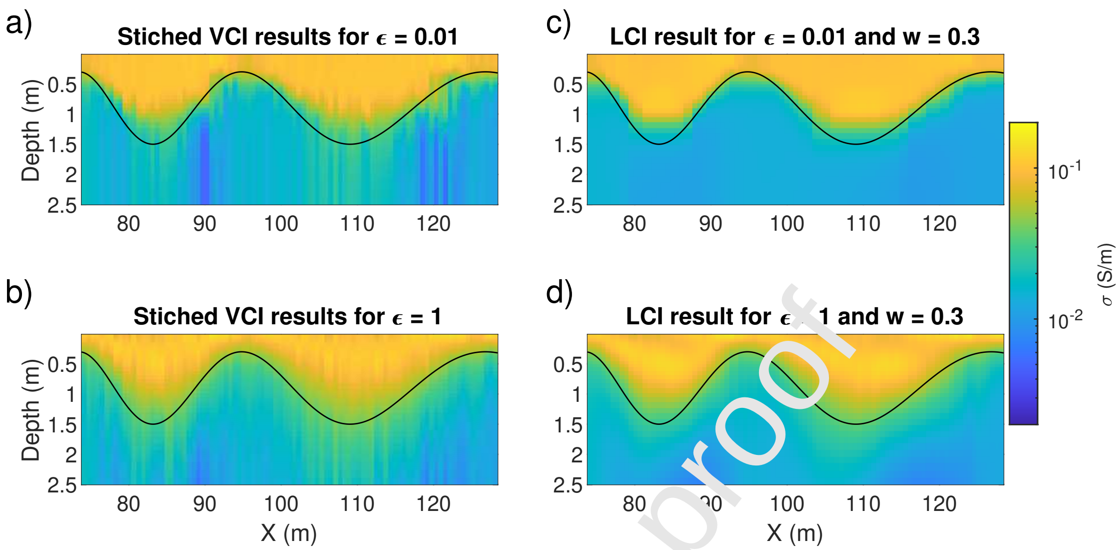

Figure 5: VCI results using (a) $\epsilon = 0.01$ and (b) $\epsilon = 1$, and LCI results using (c) $\epsilon = 0.01$ and $w = 0.3$ and using (d) $\epsilon = 1$ and $w = 0.3$. The black line indicates the true interface depth.

5. Field data example

Our field data set has been acquired in Paulinenaue, Germany, on a test site of the Leibniz Centre for Agricultural Landscape Research (ZALF). This area is characterized by peat deposits in an overall sandy environment. The peat is expected to show rather large electrical conductivities (around 0.1 S/m) and, thus, a clear contrast to the surrounding, more resistive sand. The goal of our geophysical survey is to assess the potential of the EMI method and the proposed tunable LCI approach to delineate and characterize the peat layer.

Our data have been acquired using the commercially available EMI system DUALEM-21S (Dualem Inc.). This device operates at a fixed frequency of 9 kHz and consists of four configurations, with a horizontal transmitter coil. Two horizontal receiver coils (HCP configurations) are placed in 1 m and 2 m distance and two receiver coils are placed perpendicular (PERPx configurations) respectively at 1.1 m and 2.1 m from the transmitter. During the survey, the device was mounted on a cart at a fixed height of 0.25 m above ground. The positions of the system are obtained by using a self-tracking total station (Boniger & Tronicke, 2010). In this work, we focus on one selected profile of about 50 m length with a spacing of around 0.5 m between the individual soundings. We focus on this specific profile as several push soundings (performed for measuring the peat thickness) are available.

For the inversion, we set the number of layers N_l to 50 with increasing thickness towards deeper layers up to a depth of 4 m. The assumed noise of the data $\boldsymbol{\Delta\sigma_{a,i}}$ is set to 1 mS/m which is a reasonable assumption for describing sensor noise and drift for this specific instrument (see Hanssens et al., 2021, Figure 9) as well as noise due to the instrument attitude. In Figure 6, we show a total of nine inversion results using three different values of ϵ and w. For $w = 0$, all soundings are inverted together; however, no lateral constraints are used. This can be considered similar to a VCI. However, compared to a classical single sounding VCI, here, all the soundings are jointly inverted; i.e., the inversion relies on a single global data misfit norm. In this way, all soundings can be inverted with the same number of iterations, so that the whole set of solutions shows a comparable level of sharpness.

In the shallower part of the inversion results (Figure 6), we see a low conductivity body (around 0.005 S/m) at the beginning of the profile, followed by a high conductivity body (around 0.07 S/m to 0.12 S/m) towards the right side. At depth, the conductivity is quite homogeneous and higher (around 0.02 S/m to 0.04 S/m) than inside the resistive body. A small 2D/3D data anomaly can be seen at around X = 28 m. Such short wavelength data anomaly locally yields 1D LCI models, which likely are unrealistic (2D/3D artefacts). By definition, it may be more robustly interpreted with a multi-dimensional inversion procedure (e.g., Benech et al., 2016; Guillemoteau & Tronicke, 2016; Guillemoteau et al., 2017a). In Figure 6, we interpret the shallow low conductivity body as unsaturated sand and the high conductivity body as the peat layer. The bottom part is interpreted as water-saturated sand characterized by a higher conductivity than the unsaturated sand. When comparing each inversion result in Figure 6, we notice two major features that are in agreement with our expectations: 1) The lateral consistency increases when using a higher value for w; i.e., the abrupt changes in electrical conductivity along the profile decrease with increasing w. Additionally, the 2D/3D artifact at around X = 28 m is less noticeable when using a higher value of w. 2) The level of sharpness increases with decreasing values of ϵ.

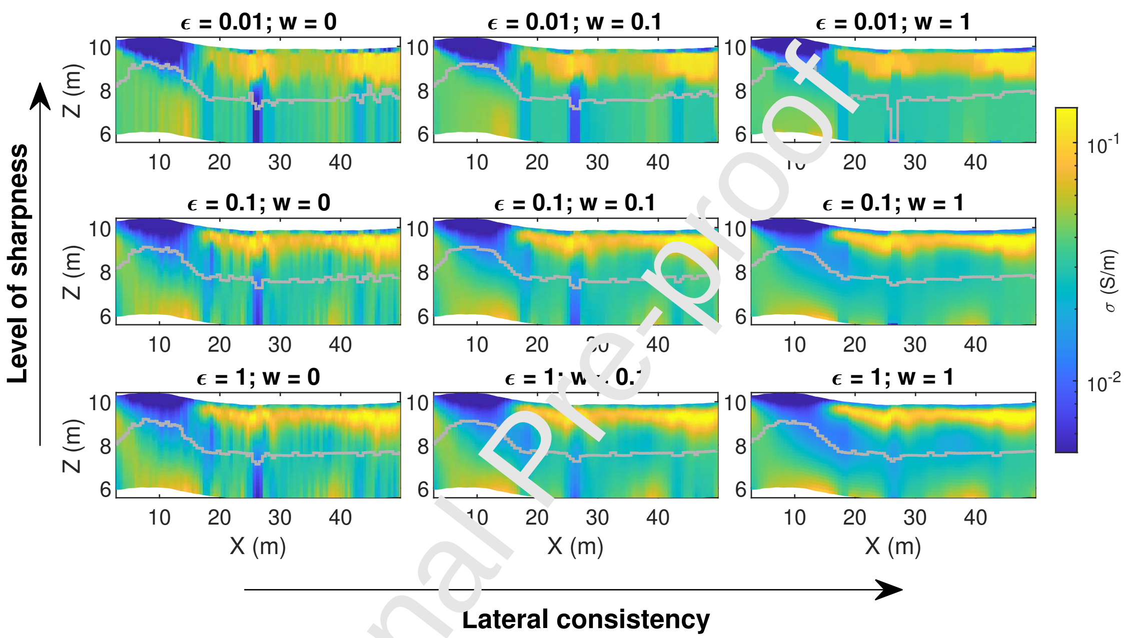

Figure 6: Results of the field data example using the LCI approach with three different values for ϵ as well as for w. All shown results have similar data misfits and can therefore be seen as equivalent solutions. The gray lines indicate an estimated maximum depth of investigation for each scenario.

All shown inversion results fit the data at the assumed level of measurement uncertainty despite having different lateral consistencies and levels of sharpness. Finding the best solution is therefore only possible with additional knowledge or (geophysical) data. For this field data set, former studies, for example borehole drillings, provide such additional knowledge. Firstly, the peat-sand-interface is expected to be sharp, and secondly, the peat layer is expected to be laterally continuous. Thus, we select the LCI case using $\epsilon = 0.01$ and $w = 1$ as the preferred solution. We analyze this result in more detail in Figure 7. In the inversion result (for clarity replicated in Figure 7a), we also show the results from the available push soundings (indicated by the black lines). The estimated peat thicknesses from these soundings are in good agreement with the selected inversion result. The RMSRE along the profile (Figure 7b) shows larger values for the first part (from X = 1 m to X = 18 m), which can be easily justified by the low σ_a values in this part. Additionally, the RMSRE curves for all other LCI results in Figure 6 are plotted in Figure 7b confirming the equivalence of all retrieved solutions in terms of data misfit. As indicated by the OP and the robust σ_a misfit plots (Figure 7c-d), the absolute differences between the observed and modeled data are equally good along the entire profile. Given the satisfactory data misfit and the excellent correlation with the results from the push soundings, the selected inversion result provides a plausible subsurface conductivity model with an easily interpretable result.

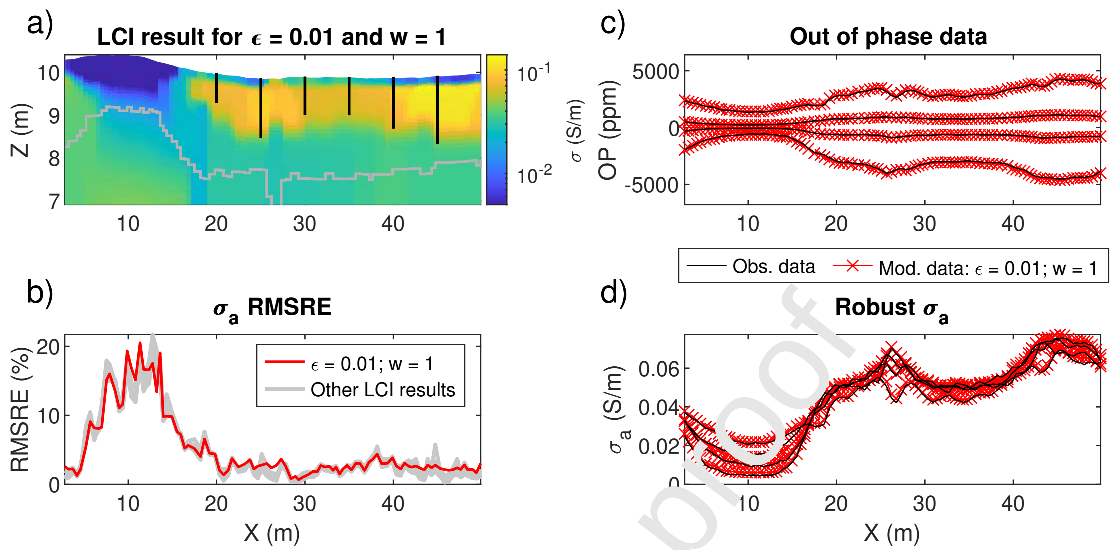

Figure 7: a) LCI result of the selected model using $\epsilon = 0.01$ and $w = 1$. The black lines indicate the estimated peat thickness obtained from push soundings. The gray line indicates an estimated maximum depth of investigation for this scenario. b) RMSRE along the whole profile of the selected model (red line) and all the other LCI results shown in Figure 6 (gray lines). c) OP data of the observed data (black line) and the modeled data (red line) from the selected model. d) Converted σ_a data of the observed data (black line) and the modeled data (red line) from the selected model.

6. Conclusions

In this work, we present a novel tunable LCI approach for FDEM data using a regularization based on the MGS method. We apply this approach to a 1D and a 2D synthetic data set and, finally, to a field data example recorded to characterize peat deposits. Our results clearly confirm that one can rather easily control the level of sharpness of the inferred model by simply acting on the focusing parameter ϵ. Using our 1D synthetic example, we also illustrate that the required number of iterations of the inversion strongly depends on the assumed noise level of the data. That means, a lower level of the assumed noise increases the number of iterations, whereby a higher number of iterations results in a higher level of sharpness in the inversion result. Our 2D synthetic example demonstrates the advantage of using lateral constraints in a quasi-layered environment. However, despite using a 2D regularization, it is important to keep in mind that the present inversion approach is based on a 1D theory. Consistently, the effectiveness of the proposed approach shows its limitations when the 1D ansatz is not met (for example on the left side of the 2D synthetic example or near X = 28 m in the field data example).

For our field data example, we generate a set of nine solutions showing distinct levels of sharpness and lateral consistency (all with similar misfit levels). For this specific survey, we aim at characterizing a rather clear boundary between a laterally extended peat deposit and the underlaying sand. In this context, we expect that the sharpest solution with a strong lateral weight is the most adapted approach. This is indeed confirmed by the push measurements available.

With our field data example, we show that our LCI approach can automatically provide (in terms of data misfit) a set of equivalent inversion results characterized by different levels of sharpness and variable lateral consistencies. It is therefore applicable for a wide range of subsurface settings. This multi-solution strategy highlights the non-uniqueness of the presented 1D LCI problem and underlines the importance of having additional complimentary data helping to find a reliable solution.

7. Acknowledgments

This project has been partially funded: by the Deutsche Forschungsgemeinschaft (DFG) (grant number 418056756); by the initiative POR-FESR Sardegna 2014-2020, Asse I Azione I.1.3 ”Creare opportunità di lavoro favorendo la competitività delle imprese” - project: ”Tecnologie di CARatterizzazione Monitoraggio e Analisi per il ripristino e la bonifica (CARMA)”. We thank Philipp Koyan and Marko Dubnitzki for collecting the EMI data set and performing the push soundings in Paulinenaue, Germany. We are also grateful to the Leibniz Centre for Agricultural Landscape Research (ZALF), in particular, to Axel

Behrendt and Gunnar Lischeid, for allowing and helping us to acquire our field data set at this test site.

References

Altdorff, D., Bechtold, M., Van der Kruk, J., Vereecken, H., & Huisman, J. (2016). Mapping peat layer properties with multi-coil offset electromagnetic induction and laser scanning elevation data. *Geoderma*, *261*, 178–189.

Auken, E., & Christiansen, A. V. (2004). Layered and laterally constrained 2D inversion of resistivity data. *Geophysics*, *69*, 752–761.

Auken, E., Christiansen, A. V., Jacobsen, L. H., & Sørensen, K. I. (2008). A resolution study of buried valleys using laterally constrained inversion of TEM data. *Journal of Applied Geophysics*, *65*, 10–20.

Auken, E., Christiansen, A. V., Kirkegaard, C., Fiandaca, G., Schamper, C., Behroozmand, A. A., Binley, A., Nielsen, E., Effersø, F., Christensen, N. B., Sørensen, K., Foged, N., & Vignoli, G. (2015). An overview of a highly versatile forward and stable inverse algorithm for airborne, ground-based and borehole electromagnetic and electric data. *Exploration Geophysics*, *46*, 223–235.

Benech, C., Dabas, M., Simon, F.-X., Tabbagh, A., & Thiesson, J. (2016). Interpretation of shallow electromagnetic instruments resistivity and magnetic susceptibility measurements using rapid 1D/3D inversion. *Geophysics*, *81*, E103–E112.

Beucher, A., Koganti, T., Iversen, B. V., & Greve, M. H. (2020). Mapping of Peat Thickness Using a Multi-Receiver Electromagnetic Induction Instrument. *Remote Sensing*, *12*, 2458.

Blaschek, R., Hördt, A., & Kemna, A. (2008). A new sensitivity-controlled focusing regularization scheme for the inversion of induced polarization data based on the minimum gradient support. *Geophysics*, *73*, F45–F54.

Boniger, U., & Tronicke, J. (2010). On the potential of kinematic GPR surveying using a self-tracking total station: Evaluating system crosstalk and latency. *IEEE Transactions on Geoscience and Remote Sensing*, *48*, 3792–3798.

Brogi, C., Huisman, J., Pätzold, S., Von Hebel, C., Weihermüller, L., Kaufmann, M., van der Kruk, J., & Vereecken, H. (2019). Large-scale soil mapping using multi-configuration EMI and supervised image classification. *Geoderma*, *335*, 133–148.

Christensen, N. B. (1995). 1D imaging of central loop transient electromagnetic soundings. *Journal of Environmental and Engineering Geophysics*, *1*, 53–66.

Christiansen, A. V., Pedersen, J. B., Auken, E., Søe, N. E., Holst, M. K., & Kristiansen, S. M. (2016). Improved geoarchaeological mapping with electromagnetic induction instruments from dedicated processing and inversion. *Remote Sensing*, *8*, 1022.

Clément, R., Pärn, J., Maddison, M., Henine, H., Chaumont, C., Tournebize, J., Uri, V., Espenberg, M., Günther, T., & Mander, Ü. (2020). Frequency-domain electromagnetic induction for upscaling greenhouse gas fluxes in two hemiboreal drained peatland forests. *Journal of Applied Geophysics*, *173*, 103944.

Constable, S. C., Parker, R. L., & Constable, C. G. (1987). Occam's inversion: A practical algorithm for generating smooth models from electromagnetic sounding data. *Geophysics*, *52*, 289–300.

Dabas, M., Anest, A., Thiesson, J., & Tabbagh, A. (2016). Slingram EMI Devices for Characterizing Resistive Features Using Apparent Conductivity Measurements: check of the DualEM-421S Instrument and Field Tests. *Archaeological Prospection*, *23*, 165–180.

Davies, G., Huang, J., Santos, F. A. M., & Triantafilis, J. (2015). Modeling coastal salinity in quasi 2D and 3D using a DUALEM-421 and inversion software. *Groundwater*, *53*, 424–431.

De Smedt, P., Van Meirvenne, M., Saey, T., Baldwin, E., Gaffney, C., & Gaffney, V. (2014). Unveiling the prehistoric landscape at Stonehenge through multi-receiver EMI. *Journal of Archaeological Science*, *50*, 16–23.

Deidda, G. P., de Alba, P. D., Rodriguez, G., & Vignoli, G. (2020). Inversion of multiconfiguration complex EMI data with minimum gradient support regularization: A case study. *Mathematical Geosciences*, (pp. 1–26).

Fiandaca, G., Doetsch, J., Vignoli, G., & Auken, E. (2015). Generalized focusing of time-lapse changes with applications to direct current and time-domain induced polarization inversions. *Geophysical Journal International*, *203*, 1101–1112.

Frederiksen, R. R., Christiansen, A. V., Christensen, S., & Rasmussen, K. R. (2017). A direct comparison of EMI data and borehole data on a 1000 ha data set. *Geoderma*, *303*, 188–195.

Grellier, S., Florsch, N., Camerlynck, C., Janeau, J. L., Podwojewski, P., & Lorentz, S. (2013). The use of Slingram EM38 data for topsoil and subsoil geoelectrical characterization with a Bayesian inversion. *Geoderma*, *200-201*, 140–155.

Guillemoteau, J., Christensen, N. B., Jacobsen, B. H., & Tronicke, J. (2017a). Fast 3D multichannel deconvolution of electromagnetic induction loop-loop apparent conductivity data sets acquired at low induction numbers. *Geophysics*, *82*, E357–E369.

Guillemoteau, J., Lück, E., & Tronicke, J. (2017b). 1D inversion of direct current data acquired with a rolling electrode system. *Journal of Applied Geophysics*, *146*, 167–177.

Guillemoteau, J., Sailhac, P., & Béhaegel, M. (2011). Regularization strategy for the layered inversion of airborne transient electromagnetic data: application to in-loop data acquired over the basin of Franceville (Gabon). *Geophysical Prospecting*, *59*, 1132–1143.

Guillemoteau, J., Sailhac, P., & Behaegel, M. (2012). Fast approximate 2D inversion of airborne TEM data: Born approximation and empirical approach. *Geophysics*, *77*, WB89–WB97.

Guillemoteau, J., Simon, F. X., Lück, E., & Tronicke, J. (2016). 1D sequential inversion of portable multi-configuration electromagnetic induction data. *Near Surface Geophysics*, *14*, 411–420.

Guillemoteau, J., & Tronicke, J. (2015). Non-standard ground conductivity meter configurations: evaluating sensitivities and applicability. *Journal of Applied Geophysics*, *118*, 15–23.

Guillemoteau, J., & Tronicke, J. (2016). Evaluation of a rapid hybrid spectral-spatial domain 3D forward modeling approach for loop-loop electromagnetic induction quadrature data acquired in low-induction-number environments. *Geophysics*, *81*, E447–E458.

Haber, E. (2014). *Computational methods in geophysical electromagnetics*. SIAM.

Hanssens, D., Vijver, E. V. D., Waegeman, W., Everett, M. E., Moffat, I., Sarris, A., & De Smedt, P. (2021). Ambient temperature and relative humidity-based drift correction in frequency domain electromagnetics using machine learning. *Near Surface Geophysics*, .

von Hebel, C., Reynaert, S., Pauly, K., Janssens, P., Piccard, I., Vanderborght, J., van der Kruk, J., Vereecken, H., & Garré, S. (2021). Toward high-resolution agronomic soil information and management zones delineated by ground-based electromagnetic induction and aerial drone data. *Vadose Zone Journal*, (p. e20099).

Jadoon, K. Z., Moghadas, D., Jadoon, A., Missimer, T. M., Al-Mashharawi, S. K., & McCabe, M. F. (2015). Estimation of soil salinity in a drip irrigation system by using joint inversion of multicoil electromagnetic induction measurements. *Water Resources Research*, *51*, 3490–3504.

Johansen, H. (1977). A man/computer interpretation system for resistivity soundings over a horizontally strafified earth. *Geophysical Prospecting*, *25*, 667–691.

Last, B., & Kubik, K. (1983). Compact gravity inversion. *Geophysics*, *48*, 713–721.

Ley-Cooper, A. Y., Viezzoli, A., Guillemoteau, J., Vignoli, G., Macnae, J., Cox, L., & Munday, T. (2015). Airborne electromagnetic modelling options and their consequences in target definition. *Exploration Geophysics*, *46*, 74–84.

Linde, N., Renard, P., Mukerji, T., & Caers, J. (2015). Geological realism in hydrogeological and geophysical inverse modeling: A review. *Advances in Water Resources*, *86*, 86–101.

McLachlan, P., Blanchy, G., & Binley, A. (2021). EMagPy: Open-source standalone software for processing, forward modeling and inversion of electromagnetic induction data. *Computers & Geosciences*, *146*, 104561.

McLachlan, P., Blanchy, G., Chambers, J. E., Sorensen, J., Uhlemann, S., Wilkinson, P. B., & Binley, A. (2020). Electromagnetic induction methods reveal wetland hydrogeological structure and properties, .

McNeill, J. D. (1980). Electromagnetic terrain conductivity measurements at low induction numbers. *Technical Note TN-6, Geonics Ltd*, .

Pérez-Flores, M. A., Antonio-Carpio, R. G., Gómez-Treviño, E., Ferguson, I., & Méndez-Delgado, S. (2012). Imaging of 3D electromagnetic data at low-induction numbers. *Geophysics*, *77*, WB47–WB57.

Portniaguine, O., & Zhdanov, M. S. (1999). Focusing geophysical inversion images. *Geophysics*, *64*, 874–887.

Rezaei, M., Saey, T., Seuntjens, P., Joris, I., Boënne, W., Van Meirvenne, M., & Cornelis, W. (2016). Predicting saturated hydraulic conductivity in a sandy grassland using proximally sensed apparent electrical conductivity. *Journal of Applied Geophysics*, *126*, 35–41.

Robinet, J., von Hebel, C., Govers, G., van der Kruk, J., Minella, J. P., Schlesner, A., Ameijeiras-Mariño, Y., & Vanderborght, J. (2018). Spatial variability of soil water content and soil electrical conductivity across scales derived from Electromagnetic Induction and Time Domain Reflectometry. *Geoderma*, *314*, 160–174.

Rudolph, S., Wongleecharoen, C., Lark, R. M., Marchant, B. P., Garré, S., Herbst, M., Vereecken, H., & Weihermüller, L. (2016). Soil apparent conductivity measurements for planning and analysis of agricultural experiments: A case study from Western-Thailand. *Geoderma*, *267*, 220–229.

Saey, T., De Smedt, P., Monirul Islam, M., Meerschman, E., Van de Vijver, E., Lehouck, A., & Van Meirvenne, M. (2012). Depth slicing of multi-receiver EMI measurements to enhance the delineation of contrasting subsoil features. *Geoderma*, *189*, 514–521.

Sasaki, Y., Kim, J.-H., & Cho, S.-J. (2010). Multidimensional inversion of loop-loop frequency-domain EM data for resistivity and magnetic susceptibility. *Geophysics*, *75*, F213–F223.

Tarantola, A. (2005). *Inverse problem theory and methods for model parameter estimation*. SIAM.

Thibaut, R., Kremer, T., Royen, A., Ngun, B. K., Nguyen, F., & Hermans, T. (2021). A new workflow to incorporate prior information in minimum gradient support (MGS) inversion of electrical resistivity and induced polarization data. *Journal of Applied Geophysics*, *187*, 104286.

Tikhonov, A. N., & Arsenin, V. Y. (1977). Solutions of ill-posed problems. *New York*, *1*, 30.

Vereecken, H., Huisman, J. A., Hendricks Franssen, H. J., Brüggemann, N., Bogena, H. R., Kollet, S., Javaux, M., van der Kruk, J., & Vanderborght,

J. (2015). Soil hydrology: Recent methodological advances, challenges, and perspectives. *Water Resources Research*, *51*, 2616–2633.

Viezzoli, A., Munday, T., Auken, E., & Christiansen, A. V. (2010). Accurate quasi 3D versus practical full 3D inversion of AEM data–the Bookpurnong case study. *Preview*, *2010*, 23–31.

Vignoli, G., Deiana, R., & Cassiani, G. (2012). Focused inversion of vertical radar profile (VRP) traveltime data. *Geophysics*, *77*, H9–H18.

Vignoli, G., Fiandaca, G., Christiansen, A. V., Kirkegaard, C., & Auken, E. (2015). Sharp spatially constrained inversion with applications to transient electromagnetic data. *Geophysical Prospecting*, *63*, 243–255.

Vignoli, G., Guillemoteau, J., Barreto, J., & Rossi, M. (2021). Reconstruction, with tunable sparsity levels, of shear wave velocity profiles from surface wave data. *Geophysical Journal International*, *225*, 1935–1951.

Vignoli, G., Sapia, V., Menghini, A., & Viezzoli, A. (2017). Examples of improved inversion of different airborne electromagnetic datasets via sharp regularization. *Journal of Environmental and Engineering Geophysics*, *22*, 51–61.

von Hebel, C., Rudolph, S., Mester, A., Huisman, J., Kumbhar, P., Vereecken, H., & van der Kruk, J. (2014). Three-dimensional imaging of subsurface structural patterns using quantitative large-scale multiconfiguration electromagnetic induction data. *Water Resources Research*, *50*, 2732–2748.

Wait, J. R. (1962). A note on the electromagnetic response of a stratified earth. *Geophysics*, *27*, 382–385.

Yi, M.-J., & Sasaki, Y. (2015). 2-D and 3-D joint inversion of loop–loop electromagnetic and electrical data for resistivity and magnetic susceptibility. *Geophysical Journal International*, *203*, 1085–1095.

Zhdanov, M., & Tolstaya, E. (2004). Minimum support nonlinear parametrization in the solution of a 3D magnetotelluric inverse problem. *Inverse problems*, *20*, 937.

Zhdanov, M., Vignoli, G., & Ueda, T. (2006). Sharp boundary inversion in crosswell travel-time tomography. *Journal of Geophysics and Engineering*, *3*, 122–134.

Zhdanov, M. S. (2002). *Geophysical inverse theory and regularization problems*. Elsevier.

Highlights

- First LCI of FDEM data using both vertical and horizontal MGS constraints
- The presented algorithm can generate pseudo-2D models of adjustable sharpness
- The generated sets of equivalent solutions highlight non-uniqueness

Declaration of interests

☒ The authors declare that they have no known competing financial interests or personal relationships that could have appeared to influence the work reported in this paper.

☐The authors declare the following financial interests/personal relationships which may be considered as potential competing interests: